

1       **Forecasting GICs and geoelectric fields from solar wind**  
2       **data using LSTMs: application in Austria**

3       **R. L. Bailey<sup>1</sup>, R. Leonhardt<sup>1</sup>, C. Möstl<sup>2</sup>, C. Beggan<sup>3</sup>, M. A. Reiss<sup>2</sup>,**  
4       **A. Bhaskar<sup>4</sup>, A. J. Weiss<sup>2,5</sup>**

5       <sup>1</sup>Conrad observatory, Zentralanstalt für Meteorologie und Geodynamik, Vienna, Austria

6       <sup>2</sup>Space Research Institute, Austrian Academy of Sciences, Graz, Austria

7       <sup>3</sup>British Geological Survey, Edinburgh, UK

8       <sup>4</sup>Space Physics Laboratory, ISRO/Vikram Sarabhai Space Centre, Trivandrum, India

9       <sup>5</sup>Institute of Physics, University of Graz, Universitätsplatz 5, 8010 Graz, Austria

10       **Key Points:**

- 11       • The aim is to directly forecast GICs rather than  $dB/dt$ , which is often used as a  
12       proxy.  
13       • Results from LSTMs predicting either  $E_x$  and  $E_y$  or substation GICs from solar  
14       wind data are compared.  
15       • GIC forecasting seems to work best when the LSTM model is trained directly on  
16       GIC data.

---

Corresponding author: Rachel Bailey, [r.bailey@zang.ac.at](mailto:r.bailey@zang.ac.at)

## 17 Abstract

18 The forecasting of local GIC effects has largely relied on the forecasting of  $dB/dt$  as a  
 19 proxy and, to date, little attention has been paid to directly forecasting the geoelectric  
 20 field or GICs themselves. We approach this problem with machine learning tools, specif-  
 21 ically recurrent neural networks or LSTMs by taking solar wind observations as input  
 22 and training the models to predict two different kinds of output: first, the geoelectric  
 23 field components  $E_x$  and  $E_y$ ; and second, the GICs in specific substations in Austria.  
 24 The training is carried out on the geoelectric field and GICs modelled from 26 years of  
 25 one-minute geomagnetic field measurements, and results are compared to GIC measure-  
 26 ments from recent years. The GICs are generally predicted better by an LSTM trained  
 27 on values from a specific substation, but only a fraction of the largest GICs are correctly  
 28 predicted. This model had a correlation with measurements of around 0.6, and a root-  
 29 mean-square error of 0.7 A. The probability of detecting mild activity in GICs is around  
 30 50%, and 15% for larger GICs.

## 31 Plain Language Summary

32 Using satellites, we measure the state of the solar wind a short distance away from  
 33 the Earth (at the so-called Lagrange-1 or L1 point) to see what is coming towards us at  
 34 any given moment. Changes in the solar wind such as an increase in wind speed or a strong  
 35 magnetic field can potentially impact satellite operation in orbit and power grid infras-  
 36 tructure on the ground - in extreme cases, solar storms can damage power grids and trans-  
 37 formers by inducing electrical currents in the power lines. These are called geomagnet-  
 38 ically induced currents (GICs). Here, we attempt to forecast the scales of GICs by ap-  
 39 plying machine learning methods, specifically Long-Short-Term-Memory recurrent neu-  
 40 ral networks, to take the solar wind data measured at the L1 point and predict the cur-  
 41 rents that would be seen in power grids in Austria. This gives us a lead time of around  
 42 10 to 40 minutes in the forecast. We discuss whether it is best to attempt to predict the  
 43 ground electric field that leads to the GICs or the GICs themselves, and discuss the dif-  
 44 ficulties in this kind of prediction and the shortfalls in the model.

## 45 1 Introduction

46 Geomagnetically induced currents (GICs) have long been known to affect power  
 47 grids, transformers and any earthed conductive networks spanning large distances (for  
 48 an overview, see Boteler et al., 1998; Boteler & Pirjola, 2017; Kelbert, 2020). GICs can  
 49 cause problems in power grid operation such as transformer overheating or permanent  
 50 transformer damage and system collapse in extreme cases (Molinski, 2002), leading to  
 51 further societal and economic harm (Eastwood et al., 2018). Although studies of GICs  
 52 were restricted to high latitudes where the consequences are more pronounced, mid-latitudes  
 53 are being paid increasingly more attention as local effects such as transformer overheating  
 54 are discovered (Barbosa et al., 2015; Butala et al., 2017; Lotz & Danskin, 2017; Gil  
 55 et al., 2019; Caraballo et al., 2020; Svanda, Michal et al., 2020, among others).

56 The forecasting of GICs has developed alongside studies into the effects of regional  
 57 GICs (Pulkkinen et al., 2006). Forecasting in particular is a complex problem due to the  
 58 chain of cascading induction effects from the impingement of solar wind at the bow shock  
 59 down to currents flowing between the earth and power grids on the surface. Improving  
 60 predictive GIC modelling is listed as one of the open questions still to address to achieve  
 61 GIC readiness (Pulkkinen et al., 2017).

62 Most studies so far have focused on predicting geomagnetic activity - such as  $dB/dt$ ,  
 63 which is often used as a proxy for GICs - from solar wind data measured at L1 or in near-  
 64 Earth space. The earliest studies addressing this problem with neural network architec-  
 65 ture are Wintoft (2005) and Wintoft et al. (2015), followed by Lotz and Cilliers (2015)

and recently Keese et al. (2020) and Tasistro-Hart et al. (2021). The  $Dst/SYMH$  index in particular has received a lot of attention from geophysicists and machine learning engineers alike (e.g. Lu et al., 2016; Bhaskar & Vichare, 2019; Wintoft & Wik, 2021).

While  $dB/dt$  is often used as a proxy for GICs, it does not provide the whole picture. The downside of modelling with this approach is that  $dB/dt$  only functions as a useful indicator of GIC activity. The relationship between  $dB/dt$  and E (which is the primary factor determining the scale of the GICs) depends on the magnetotelluric transfer function, which is frequency dependent (Chave & Jones, 2012). Single values of the time derivative of the magnetic field can only be useful GIC proxies if further assumptions on the frequency content are made (Pulkkinen et al., 2006).

What do we do if we want to develop a model that provides forecasts that power grid operators can work with? One approach would be to directly forecast the surface geoelectric field, from which GICs at different stations can be calculated. In comparison to the many studies into forecasting  $dB/dt$  and  $Dst$ , little effort has been devoted to forecasting geoelectric fields thus far. Pulkkinen et al. (2009, 2010) studied the forecasting of GICs from remote solar observations, allowing a few days warning before larger events. Modelling of geoelectric fields from solar wind to ground using full MHD modelling has been carried out by Pulkkinen, Hesse, et al. (2007), Zhang et al. (2015) and Honkonen et al. (2018), and with empirical modelling in Lotz et al. (2017).

In this study, we aim to tackle this problem from another angle and forecast regional GICs from L1 solar wind data using a machine learning method, and we compare the results to observations of GICs in Austria. We try this with two different approaches: in the first, we train a model to forecast the geoelectric field and calculate the GICs from there, and in the second we forecast the GICs directly. Predictions from both methods are evaluated and compared using data from recent years.

This study is structured as follows. Section 2 describes the data used in this study, including an analysis of 26 years of geomagnetic measurements used to model GICs in the region of Austria and a case study looking at the 2003 Halloween storm. Section 3 then goes on to describe the models built to forecast GIC values, and the results are presented in Section 4, discussed in Section 5 and summarised in Section 6.

## 2 Data

This analysis relies on INTERMAGNET-quality geomagnetic observatory data, which ensures a high quality of data with few data gaps or disturbances. We use data with a cadence of one minute because these are available for a long time period (26 years), which is not possible with 1 Hz data. Data with 1-minute resolution should be representative of most important GIC content (Pulkkinen et al., 2006). Due to Austria's small size (roughly 280 x 600 km), we assume that the geomagnetic variations are roughly constant across it both latitudinally and longitudinally, and therefore only select and use geomagnetic variations from one station at a time.

In the following, we describe the data sets used in this study. Geomagnetic field variations from observatory measurements were used to calculate the ground geoelectric field in Austria. GICs at any power grid substation can be calculated from the geoelectric field, and the equations for two specific substations are determined using a linear fit to observed GICs. In terms of the geomagnetic and geoelectric field components,  $x$  and  $y$  refer to the geographic northward and eastward directions respectively.

### 2.1 Geomagnetic observatory data from WIC and FUR

The Conrad Observatory (WIC), situated at a geomagnetic latitude of  $42.95^\circ$  and longitude of  $89.94^\circ$  according to AACGM-v2 (Shepherd, 2014), is located southwest of

114 Vienna near the town of Muggendorf in Lower Austria. High quality geomagnetic mea-  
 115 surements have been carried out here since the official opening mid-2014, providing six  
 116 years of data for analysis. We extend the time range using data from Fürstenfeldbruck  
 117 (FUR) in Bavaria, Germany. Initial studies are done using WIC data, and studies of long-  
 118 term measurements are carried out using FUR data. A map showing the location of the  
 119 two stations can be found in **Fig. 1**.

120 The Fürstenfeldbruck Geomagnetic Observatory (geomagnetic lat: 43.06°, lon: 85.93°)  
 121 is one of the closest INTERMAGNET-quality geomagnetic observatories to the Conrad  
 122 Observatory. It is situated almost directly west of WIC and separated by 348 km. This  
 123 station is a very good proxy for geomagnetic field variations in Austria due to its prox-  
 124 imity and the similar geomagnetic latitude and geological setting. Measurements at a  
 125 quality high enough for this analysis have been carried out since 1995, providing twenty-  
 126 six years of data or 13.7 million data points at a 1-minute resolution.

127 An analysis of the coherence between WIC and FUR data has been carried out for  
 128 the overlapping years of measurements (2015-2021), in which the Pearson’s correlation  
 129 coefficient (PCC) between the two time series doesn’t drop below 0.99 for either the  $x$   
 130 or  $y$  variables over all six years. The correlation in variations ( $dBx/dt$  and  $DBy/dt$ ) is  
 131 slightly lower, with the lowest values (0.91) seen in the  $DBy/dt$  values.

## 132 2.2 Geoelectric field

133 In order to model the expected levels of GICs, we need knowledge of the ground  
 134 geoelectric field in the region. The geoelectric field for the past 26 years is modelled di-  
 135 rectly from the 1-minute geomagnetic field variations at FUR. The model approach used  
 136 is the one-dimensional plane wave method (e.g. Boteler & Pirjola, 2017) using the EU-  
 137 RHOM model number 39 (Ádám et al., 2012) to describe the one-dimensional layers of  
 138 resistivity going into the Earth. We assume the time series is representative across the  
 139 country, which is a reasonable approach for small areas but not for larger countries. The  
 140 plane wave approach was used in favour of the thin-sheet approach used in previous stud-  
 141 ies (Bailey et al., 2017, 2018) for the shorter computation times with similar levels of ac-  
 142 curacy. The calculation results in the horizontal geoelectric field components  $E_x$  and  $E_y$ .  
 143 Note that the  $x$ -component in the geoelectric field corresponds to the  $y$ -component ge-  
 144 omagnetic field variations, and vice versa.

## 145 2.3 Geomagnetically induced currents

146 To evaluate the levels of GICs over the 26 years of available FUR data, we do not  
 147 follow the standard modelling procedure of putting the geoelectric field components through  
 148 the full power grid network, which would be computationally heavy, but instead find a  
 149 direct linear fit of the geoelectric field components to measurements of GICs to find the  
 150 current at station  $j$ , i.e.

$$GIC_j = a_j \cdot E_x + b_j \cdot E_y \quad (1)$$

151 where  $a_j$  and  $b_j$  are station-specific real coefficients (with units A·km/V). This approach  
 152 can only be used on transformer stations with measurements since the coefficients must  
 153 be determined from a linear fit to the data, but it often has similar or better accuracy  
 154 than results from a network model. See Pulkkinen, Pirjola, and Viljanen (2007) or Torta  
 155 et al. (2012) for more discussion on this method and for the equations determining  $a_j$   
 156 and  $b_j$ .

157 The fit for Eq. 1 was applied to measurements of direct currents from multiple trans-  
 158 former neutral points in Austrian power grid substations provided by the Graz Univer-  
 159 sity of Technology. In this study, only measurements from two substations were used:

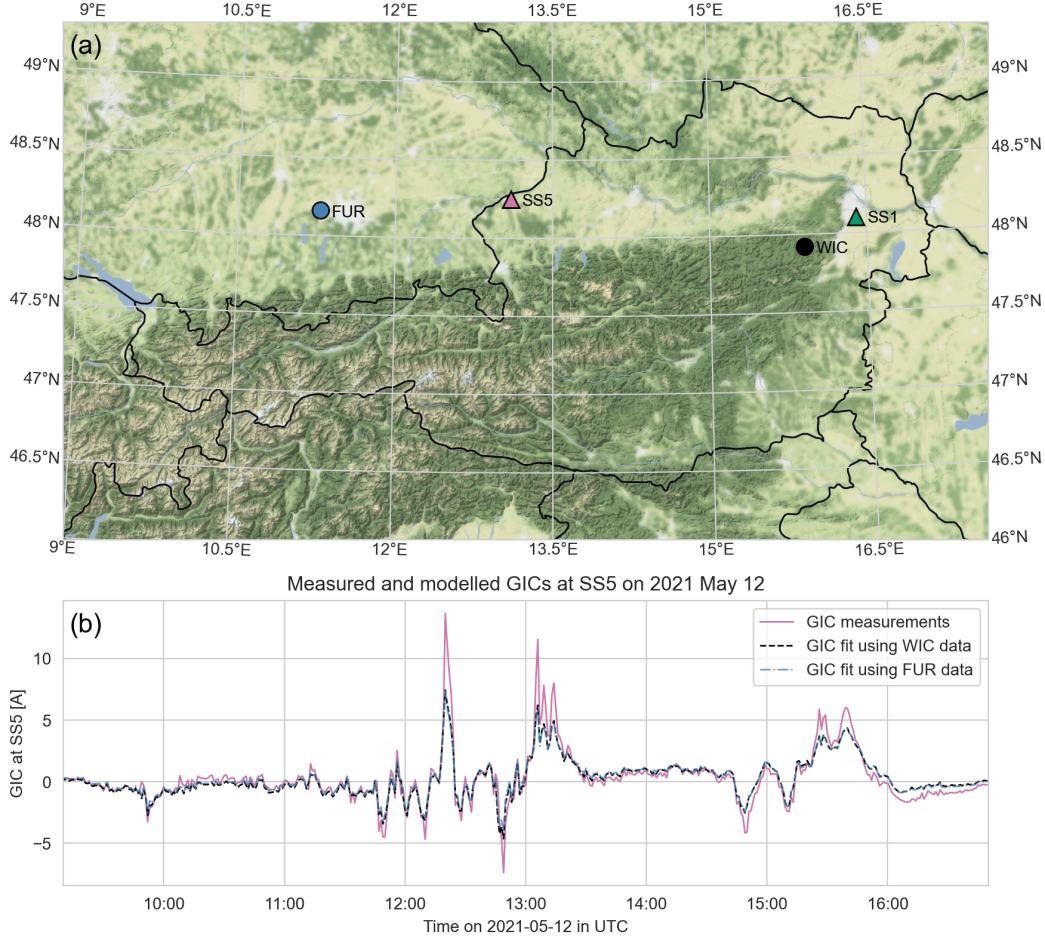


**Figure 1.** (a) A map showing the locations of two power grid substations (triangles) and the two geophysical observatories (circles) used for geoelectric field modelling, and (b) an example of GIC fit from modelled geoelectric field values for a geomagnetic storm in May 2021. The solid line (purple) shows transformer neutral point current measurements that have been offset-corrected and resampled via interpolation to a 1-minute sampling rate (from 1-second). The two dashed lines show the GICs calculated from E using WIC (black) and FUR (blue) data, which are nearly identical. Note that the largest GIC values are almost always underestimated despite the otherwise good agreement between model and measurements.

160 one near Vienna (hereafter referred to SS1 for Substation 1) and another north of Salzburg  
 161 (SS5), both with sampling rates of one second. The data was resampled to a one minute  
 162 sampling rate for use in this study using a sliding window median. These two stations  
 163 are of interest because they are in the high-voltage network and experience larger GICs  
 164 than the other stations with measurements. As such they are useful examples for depict-  
 165 ing the expected maximum scales of GICs that could be seen across the grid. We choose  
 166 three geomagnetically active periods and use the geoelectric field components  $E_x$  and  
 167  $E_y$  modelled from FUR data to derive the following equations:

$$GIC_{SS1} = 3.77 \cdot 10^{-2} \cdot E_x + 3.19 \cdot 10^{-2} \cdot E_y \quad (2)$$

$$GIC_{SS5} = 0.44 \cdot 10^{-2} \cdot E_x + 5.55 \cdot 10^{-2} \cdot E_y \quad (3)$$

168 We see that the  $x$ -component of the geoelectric field contributes roughly the same  
 169 amount to the GICs seen in SS1 as the  $y$  component. The  $y$ -component of the geoelec-  
 170 tric field mostly dominates the currents in SS5 and contributes ten times more than the  
 171  $x$ -component. The differences in contributions from geoelectric field components stem  
 172 from the varying grid layout and connections at each substation. An analysis shows that  
 173 the GICs calculated from these equations are slightly more accurate than those from the  
 174 full network model. Comparing to measurements at SS1, the Pearson's correlation co-  
 175 efficients for both GICs from the network model and GICs from Eq. 1 are 0.86, while at  
 176 SS5 the correlation improves from 0.85 to 0.88. In both cases the amplitudes of the GICs  
 177 are better matched and the root-mean-square-errors drop from 0.24 to 0.12 A at SS1 and  
 178 0.46 to 0.12 A at SS5. These measures were calculated from a fit of the geoelectric field  
 179 data to measurements using eight days of geomagnetically active periods (including the  
 180 September 2017 storm). This includes the most recent active period, meaning the mea-  
 181 surements should represent the current grid configuration and we exclude fitting only  
 182 to grid noise by using a geomagnetically active period. A fit applied to the geoelectric  
 183 field modelled from WIC rather than FUR data produces slightly different coefficients  
 184 but results in the same level of accuracy when compared to GIC measurements. An ex-  
 185 ample of the measurements and GIC fits can be seen in **Fig. 1b**.

186 Regardless of which time range the fit is applied to, the GICs calculated using Eq.  
 187 1 (as well as those from the network model) tend to underestimate the peaks of the largest  
 188 GICs by up to a factor of two (see e.g. **Fig 1b**, 12:20 or 13:05 UTC). We assume this  
 189 is a result of attenuation of the modelled geoelectric field due to the lower sampling rate  
 190 used for field modelling (Grawe et al., 2018) or the oversimplification of using a uniform  
 191 geoelectric field and 1D model of the subsurface resistivity (Ngwira et al., 2015; Sun &  
 192 Balch, 2019; Weigel, 2017). Despite this, the very good agreement between model and  
 193 measurements means that any results based on the modelled geoelectric fields will still  
 194 be reasonable.

195 In addition to the absolute GIC values, we also look at the cumulative absolute GICs  
 196 over an hour,  $GIC_{sum1h}$ .  $GIC_{sum1h}$  is taken as the sum of minute values over the hour  
 197 as a separate indicator for geomagnetic activity, more representative of sustained GICs  
 198 than large spikes, both of which can have different (but similarly detrimental) effects on  
 199 transformers (Bolduc, 2002; Gaunt & Coetzee, 2007). Using the accumulated sum of GICs  
 200 or geoelectric field has seen usage in other studies, although not often - Lotz and Dan-  
 201 skin (2017) used the accumulated E over varying periods and Viljanen et al. (2014) also  
 202 worked with daily GIC sum averaged across nodes. The scale of  $GIC_{sum1h}$  will vary de-  
 203 pending on the sampling rate of the data used, but in the case of minute data in Aus-  
 204 tria, 0 to 50 Ah can be seen during quiet times, and values above that generally repre-  
 205 sent more active times.

## 206 2.4 Distribution of values

207 In order to determine how best to forecast GICs, we first look at the 26 years of  
 208 available data and the distributions of both geomagnetic variations and modelled GICs.  
 209 **Figure 2a** presents the distribution of FUR minute  $dBx/dt$  and  $dB_y/dt$  variations. There  
 210 are very few values populating the tail of the distribution where the largest values are  
 211 found. High values for this region are at 80 nT/min and upwards. The largest variations  
 212 occur most commonly in the  $x$ -direction (leading to larger  $E_y$ ) rather than the  $y$ -direction,  
 213 implying that stations in the power grid sitting on east-west lines are already more sus-  
 214 ceptible to larger GICs.

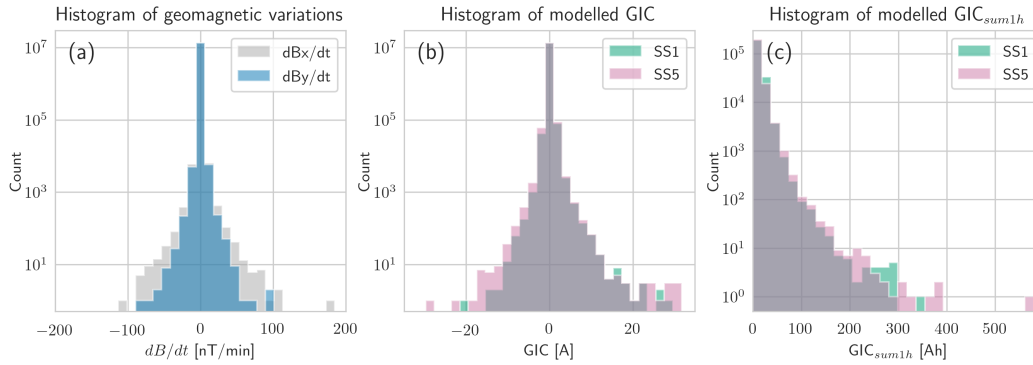


**Figure 2.** Histograms showing the distribution of the values in (a) the geomagnetic variations at FUR, (b) the GICs modelled from  $dB/dt$  at two substations, and (c) the hourly cumulative modelled GICs at two substations for all data,  $GIC_{sum1h}$ . The y-axes have logarithmic scales.

215 In **Figs. 2b and 2c**, the GICs observed at SS5 are larger than those at SS1. While  
 216 the size of the currents depends largely on the network topology and grounding resis-  
 217 tance, we noted in Section 2.3 that the currents at SS5 are mostly determined by the  $y$ -  
 218 component of the geoelectric field (or  $x$ -component of the geomagnetic field variations),  
 219 which generally sees larger variations.

## 220 2.5 Most active days

221 In **Table 1**, the 10 most active days in the 26 years of data according to different  
 222 measures of activity  $dBx/dt$  and  $dB/dt$  at FUR, modelled  $|GIC|$  and  $GIC_{sum1h}$  at both  
 223 SS1 and SS5 are listed. There are many overlapping days between the different measures,  
 224 making a total of 19 days. Bold font highlights the ten largest values in each column.

225 A similar table for largest GIC days in Central Europe was produced in Viljanen  
 226 et al. (2014, Table 4), and we see that the tables are very much in agreement with 17  
 227 shared dates, even though the table in Viljanen et al. (2014) is only based on one vari-  
 228 able. They used a value akin to the  $GIC_{sum1h}$  used here, namely the daily sum of GICs  
 229 averaged across all nodes. Similarly, 17 of the days listed here also appear in Juusola et  
 230 al. (2015), Table 3, where an analysis of the days with largest GICs was carried out for  
 231 Northern Europe. Other larger storms that have occurred since those studies (March 2015  
 232 and September 2017) do not stand out in comparison to those from the last solar cycle  
 233 with the exception of the storm from June 2015.

234 The largest values in each measure are clearly centered around the 2003 Halloween  
 235 storm. Large values in  $dBx/dt$  tend to go alongside large GIC values in SS5, and days  
 236 with large  $GIC_{sum1h}$  usually coincide with days with larger  $|GIC|$ , as expected. Some  
 237 exceptions are 2000-09-17, 2001-04-08, 2005-01-07 and 2005-08-24, which only show high  
 238 cumulative GICs but do not stand out in  $dB/dt$ -values and peak GICs. A comparison  
 239 of these events shows they have large and unidirectional geomagnetic field variations (with  
 240 total field changes of 100 to 300 nT) that occur over an hour or more. These in partic-  
 241 ular lead to sustained GICs in stations susceptible to geomagnetic field changes in that  
 242 direction. The variations on 2000-09-17 are shown as an example of this kind of behaviour  
 243 in **Fig. 3**. Although not extremely geomagnetically active, they show that power grid  
 244 transformers would have been subjected to large amounts of cumulative GICs sustained  
 245 over an hour at least.

**Table 1.** Table showing the ten most active days according to the maximum values in three measures: leftmost are the horizontal geomagnetic field variations ( $dBx/dt$  and  $dB_y/dt$ ), in the centre the absolute GICs ( $|GIC|$ ) at two different transformer stations (SS1 and SS5), and rightmost the cumulative GICs over an hour at two transformer stations ( $GIC_{sum1h}$ ). Bold font highlights the ten largest values seen in that measure. The largest values are seen during the Halloween Storm on 2003 October 29-31 (italicised).

Date	$dBx/dt$ [nT/min]	$dB_y/dt$ [nT/min]	$ GIC1 $ [A]	$ GIC5 $ [A]	$GIC1_{sum1h}$ [Ah]	$GIC5_{sum1h}$ [Ah]
1998-05-04	52.0	<b>46.0</b>	<b>11.10</b>	9.24	139.5	165.3
2000-04-06	42.9	<b>43.7</b>	9.47	11.00	176.7	192.5
2000-07-15	<b>184.7</b>	28.5	<b>17.67</b>	<b>28.39</b>	<b>265.2</b>	<b>364.5</b>
2000-09-17	34.5	19.9	10.19	8.89	<b>238.9</b>	<b>252.0</b>
2001-03-31	<b>82.4</b>	<b>40.7</b>	9.46	<b>16.69</b>	216.7	190.8
2001-11-06	<b>85.1</b>	<b>38.1</b>	<b>11.82</b>	<b>13.66</b>	<b>226.6</b>	<b>292.4</b>
2001-11-24	<b>62.4</b>	33.3	<b>12.79</b>	<b>17.42</b>	<b>262.0</b>	<b>251.6</b>
<i>2003-10-29</i>	<b>102.9</b>	<b>92.3</b>	<b>27.76</b>	<b>31.02</b>	<b>330.0</b>	<b>534.1</b>
<i>2003-10-30</i>	33.1	<b>40.3</b>	<b>16.82</b>	<b>16.69</b>	<b>268.0</b>	<b>282.6</b>
<i>2003-10-31</i>	<b>91.5</b>	<b>56.2</b>	<b>13.55</b>	<b>16.68</b>	131.8	<b>229.3</b>
2003-11-20	19.8	31.4	<b>11.90</b>	10.35	<b>284.9</b>	<b>280.3</b>
2004-07-26	<b>78.5</b>	8.5	8.74	<b>14.71</b>	77.8	77.8
2004-11-07	43.0	<b>37.7</b>	7.15	8.24	158.4	157.2
2004-11-08	24.7	28.9	<b>10.49</b>	8.64	<b>250.8</b>	212.9
2004-11-09	<b>76.1</b>	<b>49.9</b>	<b>14.99</b>	13.05	<b>261.5</b>	205.8
2005-05-15	36.3	35.1	10.38	<b>13.70</b>	<b>230.6</b>	<b>364.4</b>
2005-08-24	41.6	31.9	9.48	12.89	215.9	<b>349.1</b>
2005-09-11	<b>60.7</b>	30.7	8.04	12.07	70.8	94.1
2015-06-22	<b>63.0</b>	12.8	8.30	<b>15.85</b>	138.7	198.6

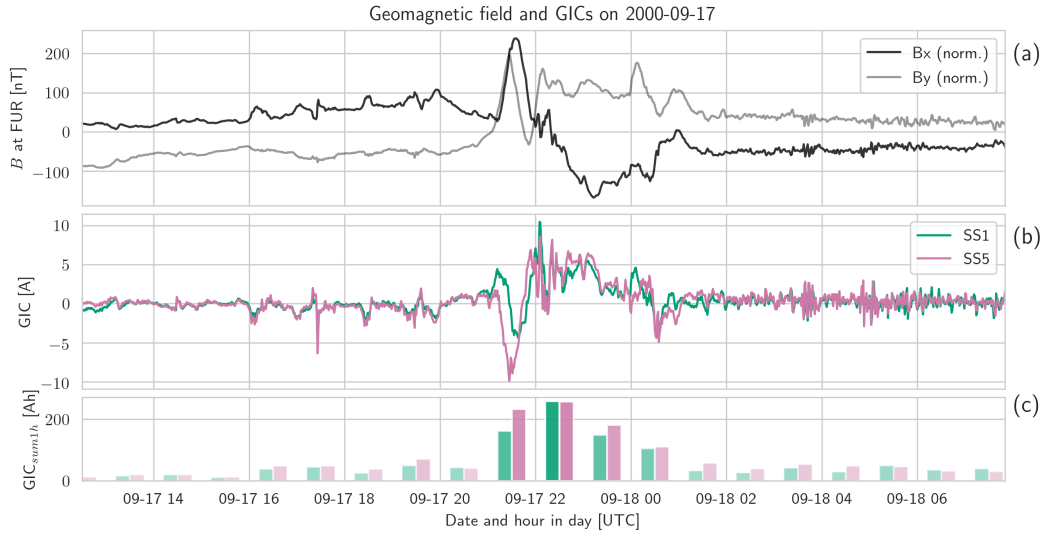


**Figure 3.** Plot of (a) geomagnetic variations at FUR (normalised to around zero by subtracting the mean field strength), (b) modelled GICs at two substations, and (c) cumulative hourly GICs on 2000-09-17 as an example of a day with no extreme GIC values but large cumulative hourly GICs.

246 **2.6 Case study: 2003 Halloween Storm**

247 In **Fig. 2**, almost all of the values in the tail end of the distribution resulted from  
 248 the ‘‘Halloween storm’’, which lasted from 2003 October 29 to November 1. These also  
 249 make up the largest values in **Table 1**, with maximum GIC values almost twice as large  
 250 as the other values seen. We now conduct a detailed analysis of the behaviour during  
 251 this storm and the GICs that were likely present in the power grid as an example of the  
 252 problems that can arise when using only  $dB/dt$  as a proxy for GICs. We see that both  
 253 large GICs and sustained GICs appear without large  $dB/dt$  values.

254 The geomagnetic storm that occurred at the end of October in 2003 was the re-  
 255 sult of a series of fast and geoeffective coronal mass ejections hitting the Earth during  
 256 a particularly active period around the maximum of solar cycle 23 (e.g., Gopalswamy  
 257 et al., 2005). In Eastwood et al. (2018), this storm was classified as a 1-in-10 year event,  
 258 and is not considered an exceptionally rare example. No event of this or a higher mag-  
 259 nitude has occurred since 2003 (with the exception of a CME directed away from Earth  
 260 on July 2012, see Ngwira et al., 2013; Baker et al., 2013; Liu et al., 2014), and such events  
 261 are somewhat more probable during the solar maxima (Owens et al., 2021), but have also  
 262 occurred at any point throughout the solar cycle.

263 A brief evaluation of this storm for Austria was carried out in Bailey et al. (2018),  
 264 in which a maximum GIC of 14 A was modelled. Using an updated model with newer  
 265 data allows us to get a more accurate estimate of GICs during stronger events, and us-  
 266 ing the method from Section 2.3 for SS1 and SS5 we see the values reaching 25–30 A.  
 267 Taking into account that the GIC peaks modelled using minute data generally under-  
 268 estimate the observations, these could also have reached up to 60 A.

269 **Figure 4** compares the geomagnetic field and the modelled GICs for the 2003 Hal-  
 270 loween Storm. Panels (a) and (b) show the geomagnetic field variations in the  $x$  and  $y$   
 271 directions. The thick lines plotted below the field show the presence of various levels of  
 272  $dB/dt$  variations (as they might be shown using a forecasting method). Light grey shows  
 273 a level of 10 nT/min, and this increases going upwards to 25 nT/min, 50 nT/min and  
 274 75 nT/min. The thickness of the line shows how often the value was exceeded within a  
 275 time frame of 30 minutes (with a maximum being 30 times). Panels (c) and (e) show the  
 276 GICs calculated from the modelled geoelectric field at the substations SS1 and SS5, and  
 277 the panels (d) and (f) show the cumulative sum of absolute GIC values ( $GIC_{sum1h}$ ) over  
 278 1-hour periods.

279 Four time intervals, highlighted in yellow on the plot, have been picked out for dis-  
 280 cussion. Intervals 1 and 2 have been selected because, as can be seen in the high levels  
 281 of  $dB/dt$  in both components, these were the most active periods. Intervals 3 and 4, in  
 282 contrast, were chosen because of continuously low levels of  $dB/dt$  but lack of higher ( $>$   
 283 50 nT/min) values.

284 Interval 1 shows a large GIC value, which is fairly short-lived. Interval 2, in con-  
 285 trast, shows a consistent level of moderate GICs, though it does not reach an extremely  
 286 high value. Interval 3 has a similar level of sustained  $GIC_{sum1h}$  as Interval 2 despite it  
 287 having a comparatively smaller amount of  $dB/dt$  over the same period. In Interval 4,  
 288 SS1 experiences the second highest value of GIC (17 A) throughout the whole storm, even  
 289 though there is only continuous low-level  $dBx/dt$  and  $dB_y/dt$  (10 to 25 nT/min), most  
 290 of it unidirectional (comparable to the type of signal seen in **Fig. 3**). On top of that,  
 291 the cumulative GICs are also some of the highest.

292 In summary, we see there are large differences between periods that have short-lived  
 293 but large GICs (Intervals 1 and 4) and those that have longer periods of sustained GICs  
 294 (Intervals 2 and 3), and both large GICs and sustained GICs can appear without large  
 295  $dB/dt$  because the ground geoelectric field responds at a range of frequencies not cap-  
 296 tured by  $dB/dt$  intensity alone. Each scenario could lead to different problems if it were

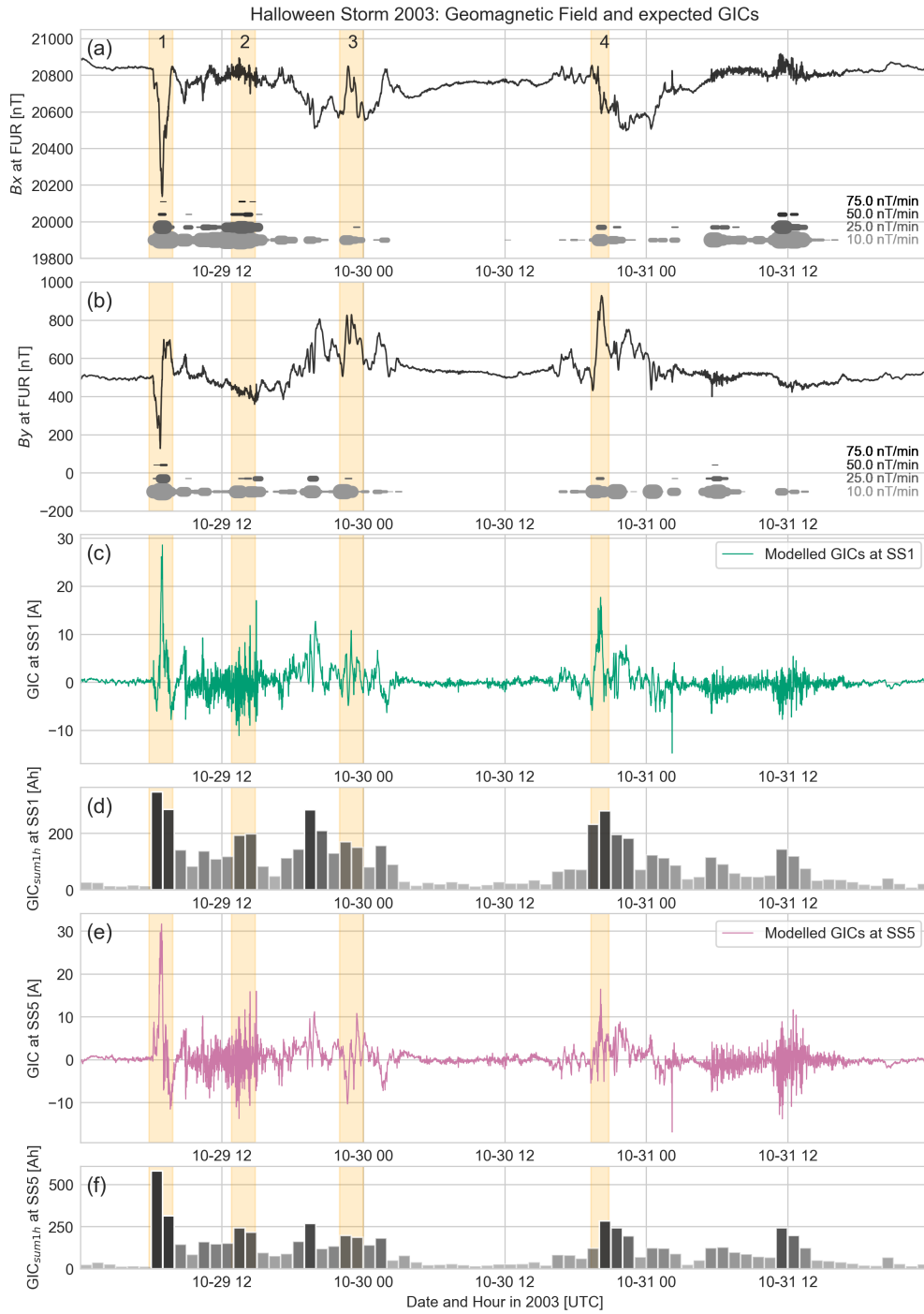


**Figure 4.** The Halloween storm from 2003 October 29 till 2003 November 1, during which some of the largest geomagnetic variations of the last few decades were seen. (a) and (b) show the geomagnetic variations at FUR in the  $x$  and  $y$  directions. Plotted below are levels of activity (10, 25, 50, and 75 nT/min) with line thickness showing how often these values were exceeded over a certain time range. (c) and (e) show the modelled GICs at the substations SS1 and SS5, and (d) and (f) show the cumulative GICs over each hour at each substation.

297 to occur in a transformer to any large degree (Price, 2002; Gaunt & Coetzee, 2007; Bolduc,  
298 2002).

### 299 3 Building a Forecasting Model

300 From the analysis of past data, we deduce that, in order to forecast a comprehen-  
301 sive summary of expected GIC behaviour, we need to forecast either both geoelectric field  
302 components or the GICs directly. While the magnitude of the field is most important,  
303 the direction also plays an important role. From Eqs. 2 and 3, we see that a large value  
304 in  $E_x$  at SS5, for example, could be cancelled out by a smaller negative one in the  $E_y$   
305 value, and the opposite could be true elsewhere, making a station-by-station approach  
306 advantageous.

307 We now move on to build a forecasting model based on these conclusions. Three  
308 machine learning methods were put through an initial comparison for evaluation: a stan-  
309 dard feed-forward neural network (NN) with three layers (32 neurons initially), a gra-  
310 dient boosting regressor based on XGBoost in Python (with 400 decision trees), and a  
311 recurrent neural network (specifically, a Long-Short-Term Memory RNN or LSTM) with  
312 three layers (32 blocks initially) and a basic Attention mechanism. sThe models were com-  
313 pared according to a set of metrics for model evaluation (root-mean-square error, Pear-  
314 son’s correlation coefficient, probability of detection). From these first comparisons, the  
315 LSTM with Attention showed the most promise and was developed into the final model,  
316 although due to the myriad machine learning methods available these days there may  
317 well be other approaches equally suited for this task.

#### 318 3.1 Data preparation

319 The input to the machine learning model is solar wind data measured at L1 and  
320 forward-propagated to the bow shock. This means that, assuming we take measurements  
321 from satellites situated at L1, we have a varying forecast lead time between 15 and 60  
322 minutes depending on the solar wind speed. The high resolution OMNI data set (see sec-  
323 tion on Data Availability for details) was used for solar wind measurements (speed, den-  
324 sity, and magnetic field components) at a minute cadence combined with the local time  
325 and day in year to make up the features, while the model target was either the geoelec-  
326 tric field (E) modelled from FUR data or the GICs modelled from the  $E_x$  and  $E_y$  com-  
327 ponents.

328 Taking solar wind measurements that have already been propagated forward to the  
329 bow shock, we use the two hours prior to the time we wish to forecast as input. This goes  
330 from  $t - 120$  minutes to  $t - 0$ , where  $t$  is the forecast time. The range of 120 minutes  
331 for past data was decided on through experimentation, where the period was increased  
332 until longer periods did not lead to any improvements in the forecasting skill. To reduce  
333 the size and complexity of the input data, it is subsampled to a 10-minute resolution by  
334 picking every 10th point (rather than interpolation and/or fitting, which we found led  
335 to a loss in forecast skill), resulting in sequences of length 12. These sequences are used  
336 as input to forecast the maximum value of E or GICs over 40 minutes from  $t - 10$  to  
337  $t+30$ . This step of ten minutes into the “past” (which reduces the lead time by ten min-  
338 utes) is to account for possible timing errors in propagating the solar wind forward to  
339 the bow shock.

340 Sampling the modelled geoelectric field or GIC data to produce a balanced data  
341 set for model training is challenging because there is a clear bias towards quiet times and  
342 not enough data from geomagnetically active times (with a factor of roughly  $10^7 : 1$   
343 for quiet to active). An initial approach using the entire data set led to a trained model  
344 that predicted only quiet times, which could not be remedied without additional data  
345 handling or large changes to the training methods. The target data set was therefore se-

346 lectively sampled to reduce the imbalance. The distribution of samples was undersam-  
 347 pled in the range of  $E = 0$  to  $100$  mV/km ( $GIC = 0$  to  $8$  A). Above that, we applied  
 348 some data augmentation by duplicating the samples by 2 to 5 times and applying a ran-  
 349 dom offset in time to the input data of each to avoid identical samples. The offset was  
 350 randomly sampled without replacement from values between  $-10$  and  $+10$  minutes, which  
 351 shifts the input solar wind data that the model sees, and means that the maximum value  
 352 was either closer to the start or the end of the following 40-minute forecast window. Oth-  
 353 erwise, all samples had a minimum time difference of 60 minutes between them. The re-  
 354 sulting distribution is close to a one-sided Gaussian distribution. Roughly the same num-  
 355 ber of samples (9000) were used in training for each target.

356 The samples were split into training and testing sets by time. The years 2000, 2001  
 357 were reserved for validation to aid in model selection during training, while 2017, 2019  
 358 and 2020 were reserved for testing, and the remaining 21 years were used in training. The  
 359 presence of data gaps longer than 15 consecutive minutes in the OMNI data set led to  
 360 samples being excluded from the analysis - this led to 8 to 15% sample exclusion, depend-  
 361 ing on the years used. Data gaps shorter than 15 minutes were linearly interpolated over.

362 We reduced all values of  $E > 200$  mV/km ( $GIC > 15$  A) to  $200$  mV/km ( $15$  A)  
 363 because the larger values were only present in roughly 100 of the 13.7 million time-steps  
 364 (or five to seven events in the 25-year period) and heavily skewed the distribution, in which  
 365 all values were scaled between 0 and 1. Rescaling points above this limit greatly improved  
 366 the level to which the model could learn the problem but also means that the maximum  
 367 forecast the model can realistically produce is for  $200$  mV/km.

### 368 3.2 Training the LSTM

369 To approach this forecasting problem, we use a four-layer LSTM with an Atten-  
 370 tion layer. The Attention mechanism is meant to simulate human attention (first devel-  
 371 oped in Bahdanau et al., 2015), which can be understood intuitively as a mechanism that  
 372 picks out the most important part of a sequence and discards the parts that are consid-  
 373 ered irrelevant. It is a tool now commonly applied in natural language processing for ex-  
 374 ample (Galassi et al., 2020). The model is structured so that the input first goes through  
 375 an LSTM layer and then through the Attention mechanism. The data is then fed into  
 376 another LSTM layer before going through a final feed-forward layer to reduce the out-  
 377 put to a single value.

378 For geoelectric field prediction, the LSTM branches into two: the left side deals with  
 379 a regression problem, namely forecasting the maximum magnitude of the geoelectric field.  
 380 We chose a custom loss function for the regression problem where events (peaks) are rare  
 381 in the data, and where the scale of the peaks is important. A min-max scaling factor used  
 382 as a penalty term meant that training to match the peak value would drive the loss down.  
 383 The right side of the LSTM forecasts the sign of the geoelectric field in a classification  
 384 problem, which in this case is the sign of the maximum field value used for the regres-  
 385 sion problem. Here, the binary cross-entropy loss function was used. Training worked  
 386 better when the two were trained as separate targets, rather than attempting to fore-  
 387 cast  $E$  without taking the absolute value first. The regression problem appears to be not  
 388 too difficult a task, but the model had far more problems trying to forecast the direc-  
 389 tion. In training, the weights of the two problems are, when scaled, about  $15 : 1$  for re-  
 390 gression to classification. The classification problem to determine the sign is given sec-  
 391 ondary importance because even an LSTM dedicated to this problem had trouble achiev-  
 392 ing a good level of accuracy. A diagram of the different LSTM architectures, the loss func-  
 393 tions and the hyperparameters used for the training of each model can be found in the  
 394 supporting information. Iteration through the various possible hyperparameters was car-  
 395 ried out for all four models for optimisation. Similar sets of hyperparameters were found  
 396 for each LSTM application, with some minor differences between them, although the choice

397 of the same hyperparameters for all applications also led to reasonable models in all cases.  
 398 Regularisation was applied in the form of dropout.

399 Multiple models were trained to evaluate the best approach for forecasting GICs.  
 400 Those trained to forecast the geoelectric field components are referred to as LSTM-E,  
 401 while nets trained to forecast the GICs directly are referred to as LSTM-GIC. Both neu-  
 402 ral nets are only trained on the output of geophysical models (in the case of E, the re-  
 403 sult of FUR variations put through the plane-wave model, and for GICs, these are the  
 404 currents calculated in power grid transformers from E) because we don't have measure-  
 405 ments of E or GIC over long enough periods and because, as described in Sec. 2.3, GICs  
 406 from geophysical models reach a good enough accuracy to be a reasonable substitute in  
 407 training. Both models predict the absolute value of the target, but the LSTM-E predicts  
 408 the sign (positive or negative) in addition.

### 409 3.3 Evaluating the model skill

410 Each model was trained on its respective training set and the best LSTM param-  
 411 eters were chosen based on model behaviour when presented with the validation set. Fol-  
 412 lowing training, we ran the model on the test data set in a virtual ‘real-time mode’ pro-  
 413 viding updates to the input data every 15 minutes, and giving an output with a 15-minute  
 414 cadence. The comparison to the ground truth (either the modelled geoelectric field or  
 415 measured GICs) is performed point-to-point as well as by looking at events, where the  
 416 event-based analysis is given the most importance. In order to have a benchmark for com-  
 417 parison, we produced a real-time persistence approach which takes the maximum of the  
 418 geoelectric field or GICs in the 20 minutes before the solar wind measurement time to  
 419 forecast the maximum when the solar wind would reach Earth. As such, the persistence  
 420 model (PERS) also uses a varying forecast lead time. The machine-learning forecast model  
 421 should be able to beat persistence in most measures.

422 Our event-based analysis follows the recommendations put forward by Pulkkinen  
 423 et al. (2013) and Welling et al. (2018) for  $dB/dt$  forecasting. An “event” in the data is  
 424 classified as a value that exceeds a certain threshold, while all values below that thresh-  
 425 old are non-events. By defining a threshold, we can calculate the confusion matrix (Wilks,  
 426 2011), which includes the number of correctly-predicted events or true positives (TP),  
 427 missed events or false negatives (FN), incorrectly-predicted events or false positives (FP),  
 428 and the correctly-predicted non-events or true negatives (TN). The metrics proposed in  
 429 Pulkkinen et al. (2013) include the Probability of Detection (POD), which is the frac-  
 430 tion of measured events correctly predicted as events, also called the true positive rate  
 431 (TPR or  $TP/(TP+FN)$ ). Similarly, we include the probability of False Detection (POFD),  
 432 the fraction of measured non-events incorrectly predicted as events, which is equivalent  
 433 to the false positive rate (FPR or  $FP/(FP+TN)$ ). In addition, the Heidke Skill Score (HSS)  
 434 and True Skill Statistic (TSS) are also considered, both of which are derived from all vari-  
 435 ables in the confusion matrix (see e.g. Heidke, 1926; Bloomfield et al., 2012). Both the  
 436 HSS and TSS show no model skill at 0, and better model skill when approaching 1. The  
 437 TSS has the benefit over the HSS of being unbiased by event/non-event ratios. We also  
 438 include the bias (BS), which shows if the model tends to over-predict (more false posi-  
 439 tives,  $BS > 1$ ) or under-predict (more false negatives,  $BS < 1$ ).

## 440 4 Results

441 We present the results split in two parts: in the first part, we test our model’s fore-  
 442 casting ability with regards to the the geoelectric field components. The results are com-  
 443 pared to the geoelectric field modelled from geomagnetic variations at FUR (see Sec. 2.2).  
 444 In the second part, we test the forecasting ability for GICs. These are calculated using  
 445 (1) the geoelectric field components predicted from LSTM-E to calculate the GICs at  
 446 the two substations we picked for analysis, and (2) directly from LSTM-GIC for each sub-

447 station. The comparison between the model results and measurements of GICs is car-  
 448 ried out for the years 2017, 2019 and 2020.

449 For the evaluation of geoelectric field forecast, we compute the scores for three event  
 450 thresholds: these are 30, 60, and 90 mV/km in both  $E_x$  and  $E_y$ . In GICs, the level of  
 451 60 mV/km corresponds to a current of roughly 4 A through either SS1 or SS5, and we  
 452 use similar thresholds of 2, 4 and 6 A. It is difficult to determine the minimum level of  
 453 GICs above which transformers may experience adverse effects because these are heav-  
 454 ily dependent on transformer type and the presence of DC-handling mechanisms. We  
 455 have too few measurements of GICs exceeding higher levels such as 10 A to make an anal-  
 456 ysis at this level useful, but 4 A is crossed often during geomagnetically active times. The  
 457 results are described in the next section.

458 **Figure 5** gives a graphical representation of the model behaviour at each thresh-  
 459 old using receiver-operator characteristic (ROC) and detection-error tradeoff (DET) curves.  
 460 Both depict the model's ability to forecast events at varying thresholds. The ROC curve  
 461 shows the trade-off between the true positive rate (also POD) and false positive rate (also  
 462 POFD) at different event thresholds. Usually, when the threshold is low, the TPR is high  
 463 but we also see an increased FPR, which is unwanted - a model that captures the ob-  
 464 served behaviour shows a curve that keeps close to the upper left corner. The area-under-  
 465 the-curve (AUC in the legend) shows good model skill as it approaches 1. On the other  
 466 hand, the DET curve shows the relationship between the false negative rate (fraction of  
 467 all predicted non-events that were measured events misclassified as non-events, or  $FN/(FN+TN)$ )  
 468 and false positive rate, the number of which usually goes up as the other goes down de-  
 469 pending on where the threshold for an event is set. Here, the best model behaviour is  
 470 seen as the curves approach the lower left corner. It is useful in error minimisation to  
 471 deduce the rate at which the FNR improves with regards to an increase in FPR rate (and  
 472 vice-versa).

#### 473 4.1 Forecasting $E_x$ and $E_y$

474 We first evaluate the LSTMs trained on the geoelectric field in terms of the root-  
 475 mean-square-error (RMSE) and the Pearson's correlation coefficient (PCC). Compar-  
 476 ing the LSTM-E outputs to modelled  $E$ , the RMSE values are 126 mV/km and 111 mV/km  
 477 for the absolute value of  $E_x$  and  $E_y$ , while the PCC values are 0.60 and 0.61. Once the  
 478 sign of  $E$  has been included, the RMSE rises to 261 mV/km and 287 mV/km, while PCC  
 479 drops to 0.48 and 0.32, so we see that the model's inability to forecast the field direc-  
 480 tion reliably decreases the accuracy when also considering the field direction.

481 **Table 2** presents an event-based analysis of the LSTM-E results. Multiple thresh-  
 482 olds (TH) defining events were considered, and these are listed by the variable "TH" in  
 483 each line (at 30, 60, and 90 mV/km, representing minor, moderate and strong geomag-  
 484 netic activity). We see that the skill decreases as the threshold increases (decreasing prob-  
 485 ability of detection POD and TSS), and that the LSTMs tend towards over-predicting  
 486 ( $BS > 1$ ). (The bias for the PERS models is always  $\sim 1$  because the time series being  
 487 compared are only shifted in time and therefore almost statistically equivalent.) There  
 488 are always a large number of false positives, although this remains a small fraction of  
 489 the number of total data points. The LSTM-E models generally outperform the PERS  
 490 approach, although the Heidke Skill Scores are occasionally smaller in the LSTMs, which  
 491 implies a worse balance between false positives and true positives. As in the point-to-  
 492 point values, the  $E_x$  component tends to be predicted better than the  $E_y$  component.  
 493 By evaluating the ROC and DET curves in Fig. 5 (a-b), we see that the LSTM-E mod-  
 494 els outperforms persistence at all thresholds.

495 We also conducted a comparison with the results from Honkonen et al. (2018) and  
 496 Lotz and Danskin (2017), where possible. While the time development of the geoelec-  
 497 tric field appears better in the modelling approach in Honkonen et al. (2018), the mag-

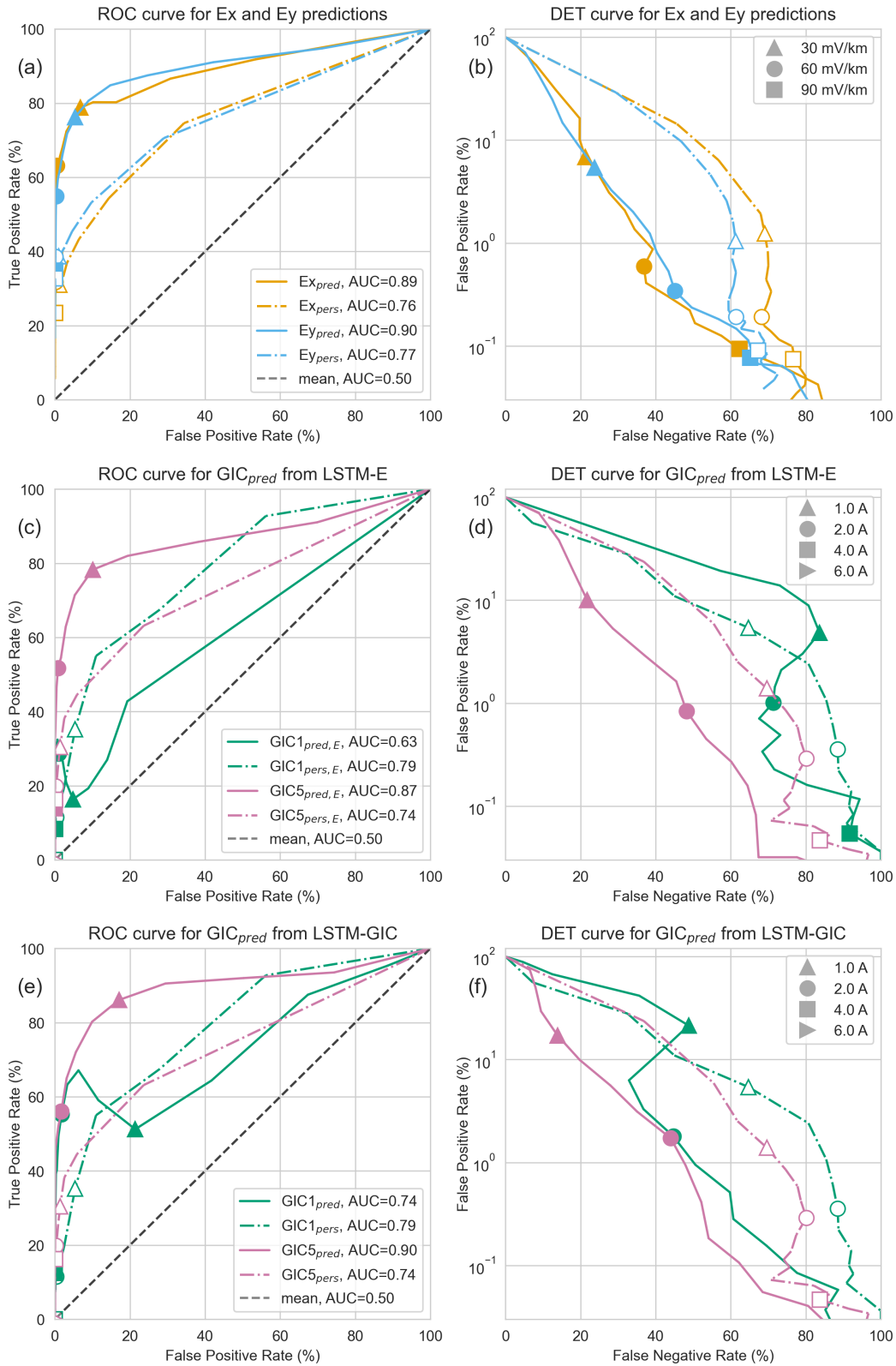


**Figure 5.** Receiver-operator characteristic (ROC) and detection-error tradeoff (DET) curves for three approaches: (a-b) the geoelectric field, showing the output from the LSTM-E models vs the modelled geoelectric field, (c-d) the GICs calculated from the geoelectric field predicted by LSTM-E compared to measured GICs, and (e-f) the GICs predicted by the LSTM-GIC models compared to measured GICs. SS1 and SS5 are two separate substations in the power grid from which we have measurements. The values for specific event thresholds are labelled with shapes as defined in each legend.

**Table 2.** Metrics from an event-based analysis of the LSTM-E models applied to the years 2000, 2001, 2017, 2019 and 2020 in a retrospective real-time mode with the model being run at 15-minute intervals. A persistence model (PERS) is included for comparison. The first four columns provide the values for the confusion matrix (where TP, FP, TN and FN are the true positives (hits), false positives, true negatives (misses) and false negatives), the probability of detection (POD), probability of false detection (POFD), Heidke Skill Score (HSS), True Skill Score (TSS), and bias (BS). The variable TH in brackets gives the event threshold used to define events and compute the metrics.

LSTM-E Model	$N_{events,obs}$	TP	FP	FN	TN	POD	POFD	HSS	TSS	BS
$E_{X,pred}(TH=30)$	3092	2436	11749	656	160506	78.8	6.8	0.26	0.72	4.6
$E_{X,pred}(TH=60)$	494	312	1038	182	173815	63.2	0.6	0.34	0.63	2.7
$E_{X,pred}(TH=90)$	175	66	164	109	175008	37.7	0.1	0.33	0.38	1.3
$E_{Y,pred}(TH=30)$	2989	2279	9328	710	163030	76.2	5.4	0.29	0.71	3.9
$E_{Y,pred}(TH=60)$	559	307	600	252	174188	54.9	0.3	0.42	0.55	1.6
$E_{Y,pred}(TH=90)$	241	84	135	157	174971	34.9	0.1	0.36	0.35	0.9
PERS Model	$N_{events,obs}$	TP	FP	FN	TN	POD	POFD	HSS	TSS	BS
$E_{X,pers}(TH=30)$	3092	958	2128	2134	170127	31.0	1.2	0.30	0.30	1.0
$E_{X,pers}(TH=60)$	494	157	335	337	174518	31.8	0.2	0.32	0.32	1.0
$E_{X,pers}(TH=90)$	175	41	130	134	175042	23.4	0.1	0.24	0.23	1.0
$E_{Y,pers}(TH=30)$	2989	1156	1804	1833	170554	38.7	1.0	0.38	0.38	1.0
$E_{Y,pers}(TH=60)$	559	216	335	343	174453	38.6	0.2	0.39	0.38	1.0
$E_{Y,pers}(TH=90)$	241	79	158	162	174948	32.8	0.1	0.33	0.33	1.0

518 nitudes are not matched as well. An event-based analysis could not be carried out in their  
519 case due to the short time series and lack of larger events, but the RMSE and PCC val-  
520 ues for  $E_X$  and  $E_Y$  (reduced to a 15-min sampling rate) come out as 10.5 mV/km and  
521 97.8 mV/km and 0.62 and 0.25, respectively, which is better in the case of  $E_X$  but worse  
522 in the case of  $E_Y$ . Comparing to Lotz and Danskin (2017), we see similar correlations  
523 for the geoelectric field components. They found a slightly higher correlation (averaged  
524 over three stations and two storms, 0.71 for  $E_X$  and 0.53 for  $E_Y$ ), although they predicted  
525 the maximum value for a longer time span (90 mins), making their approach closer to  
526 a nowcast than a forecast. The higher RMSE values seen in our study in part derive from  
527 the slightly higher levels of daily variation that is forecast even when the field is extremely  
528 quiet. Again, in both studies used as comparison we see the northward component of the  
529 geoelectric field was predicted better than the eastward component.

## 510 4.2 Forecasting GICs

511 The same results are presented for GICs as for the geoelectric field components in  
512 the last section. In the event-based analysis, the thresholds were set at 2, 4 and 6 A, which  
513 are roughly equivalent to the thresholds used for the electric field. **Table 3** shows the  
514 results of this analysis applied to the test data set years 2017, 2019 and 2020, while **Fig. 5**  
515 depicts the ROC and DET curves for the model output versus measured GICs. A com-  
516 parison between the LSTM-GIC output and the modelled GICs the model was trained  
517 on shows similar levels of accuracy as in LSTM-E to the geoelectric field.

518 We first look at the results for GICs calculated from the geoelectric field compo-  
519 nents predicted using the LSTM-E models. Note that while the last section mainly looked  
520 at the absolute value of the geoelectric fields, in the calculation of GICs the direction of

**Table 3.** Metrics from an event-based analysis of different model applied to the years 2017, 2019 and 2020 in a retrospective real-time mode with the model being run at 15-minute intervals.  $GIC1_{pred,E}$  is the result from the models trained to predict the geoelectric field (LSTM-E), while  $GIC1_{pred}$  is the result from the LSTM-GIC. PERS is a persistence model assuming the target (GIC) repeats itself. The first four columns provide the values for the confusion matrix (where TP, FP, TN and FN are the true positives (hits), false positives, true negatives (misses) and false negatives), the probability of detection (POD), probability of false detection (POFD), Heidke Skill Score (HSS), True Skill Score (TSS), and bias (BS). The variable TH in brackets is the event threshold used to define events and compute the metrics. "undef." refers to the HSS and TSS at TP=0, which are undefined.

LSTM-E Model	$N_{events,obs}$	TP	FP	FN	TN	POD	POFD	HSS	TSS	BS
$GIC1_{pred,E}(TH=2)$	432	124	1060	308	103697	28.7	1.0	0.15	0.28	2.7
$GIC1_{pred,E}(TH=4)$	24	2	57	22	105108	8.3	0.1	0.05	0.08	2.5
$GIC5_{pred,E}(TH=2)$	307	159	681	148	80649	51.8	0.8	0.27	0.51	2.7
$GIC5_{pred,E}(TH=4)$	43	6	13	37	81581	14.0	0.0	0.19	0.14	0.4
LSTM-GIC Model	$N_{events,obs}$	TP	FP	FN	TN	POD	POFD	HSS	TSS	BS
$GIC1_{pred}(TH=2)$	432	239	1886	193	102871	55.3	1.8	0.18	0.54	4.9
$GIC1_{pred}(TH=4)$	24	3	26	21	105139	12.5	0.0	0.11	0.12	1.2
$GIC5_{pred}(TH=2)$	307	172	1403	135	79927	56.0	1.7	0.18	0.54	5.1
$GIC5_{pred}(TH=4)$	43	7	16	36	81578	16.3	0.0	0.21	0.16	0.5
PERS Model	$N_{events,obs}$	TP	FP	FN	TN	POD	POFD	HSS	TSS	BS
$GIC1_{pers}(TH=2)$	432	50	375	382	104382	11.6	0.4	0.11	0.11	1.0
$GIC1_{pers}(TH=4)$	24	0	26	24	105139	0.0	0.0	undef.	undef.	1.1
$GIC5_{pers}(TH=2)$	307	61	237	246	81093	19.9	0.3	0.20	0.20	1.0
$GIC5_{pers}(TH=4)$	43	7	38	36	81556	16.3	0.0	0.16	0.16	1.0

521 the geoelectric field is also included, making this an additional error factor if the sign  
522 is not predicted accurately. Once the GICs have been calculated using the results from  
523 the LSTM-E models and Eq. 1, the absolute value is taken for the rest of the analysis.

524 As can be seen in **Table 3**, the GICs derived from the LSTM-E models see a con-  
525 siderable drop in accuracy in comparison to the results for E alone in Table 2. Although  
526 there were quite reasonable values for POD predicting E, the POD for GICs at the mid-  
527 range threshold (60 mV/km or 4 A) drops from around 50% in both components of E  
528 to 8% and 16% in substation SS1 and SS5. Evaluating the skill of the model for GICs  
529 at high levels is difficult because there are so few events exceeding even a minimal value  
530 of 6 A. None of these events (2 at SS1, 12 at SS5 over the three years of data) were pre-  
531 dicted using any approach.

532 In comparing the GIC predictions from the two methods (LSTM-E and LSTM-GIC),  
533 we see that the LSTM-GIC seems to perform better but the results are station-specific.  
534 The LSTM-GIC performs much better than the LSTM-E at SS1 (e.g. a POD of 55% rather  
535 than 29% and higher HSS and TSS values at a threshold of 2 A) and at a similar level  
536 at SS5. This is also reflected in a model evaluation using point-to-point metrics. The RMSE  
537 values for SS1 and SS5 predicted using LSTM-E are 0.49 A and 0.59 A, while the PCC  
538 is 0.35 and 0.67. For GICs predicted using LSTM-GIC, the RMSE values are 0.67 A and  
539 0.78 A (i.e. slightly worse than LSTM-E), but the PCC is 0.56 and 0.64. The accuracy  
540 between the two approaches is roughly equivalent for SS5, but using LSTM-GIC rather

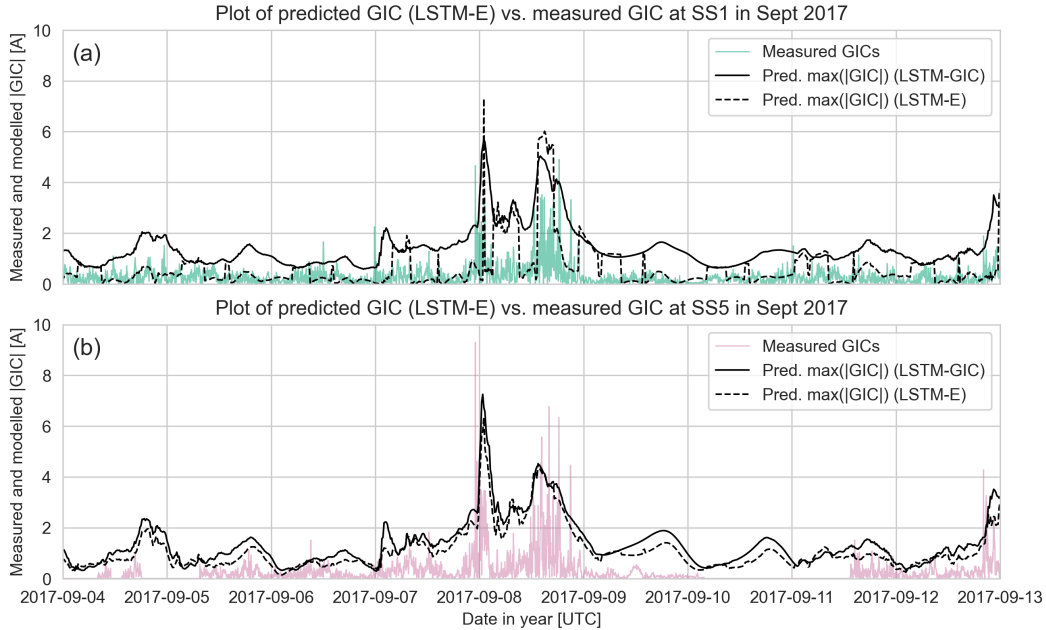


**Figure 6.** The LSTM-E (dashed line) and LSTM-GIC (solid line) applied to forecasts in an experimental real-time mode and compared to measurements of GICs (coloured lines) at two stations in Austria. The upper panel (a) shows results for SS1 near Vienna, while the lower panel (b) shows results for SS5 near Salzburg (with some data gaps). Although not plotted here, the maximum GIC value computed from the measurements is at the same cadence of 15 minutes to compare to the model forecasts.

541 than LSTM-E is a definite improvement for SS1 observations. Some of the reason for this  
 542 can be seen in **Fig. 6**. In SS1, the jumps in values computed from LSTM-E result from  
 543 changes in the sign of the geoelectric field components, which then cancel each other out  
 544 and lead to a GIC of zero. (Conversely, ignoring the sign from LSTM-E and taking the  
 545 absolute values to calculate the GICs in SS1 results in higher correlation and POD but  
 546 a far larger number of false positives, leaving this as another possibility.) In the best cases,  
 547 the GIC forecasts only reach a POD of 16% for GICs above a threshold of 4 A, highlight-  
 548 ing the difficulty in correctly predicting larger values.

549 In the ROC and DET curves in **Figure 5** panels (c-d) for GICs from LSTM-E and  
 550 (e-f) from LSTM-GIC, we also see some of the weak forecasting ability for SS1 primar-  
 551 ily represents the LSTM behaviour at low values (GICs < 1 A). At SS1, there is a mostly  
 552 continuous level of noise around 1 A, and the model does not predict the noise while the  
 553 persistence model captures it clearly. This is an example of the weakness of ROC curves,  
 554 where in this case only the lower left corner (showing values greater than 1 A) is of in-  
 555 terest to us.

556 **Figure 6** shows the forecast that would have been produced by the model (solid  
 557 and black dashed lines) against measurements (coloured lines) during the September 2017  
 558 storm. The models, particularly the LSTM-GIC approach, do a reasonable job at pred-  
 559 icting magnitudes, although the LSTM-E struggles to predict the direction, which is  
 560 also important for accurate GIC prediction. The storm and the active periods are clearly  
 561 captured by the forecast, and daily variations from the Sq current are forecasted oth-  
 562 erwise. Note that the delayed rise in the forecast of the first peak of the storm does not  
 563 indicate a timing error. A cross-correlation of the model output shows at maximum an

564 offset in time of 10 minutes and the delay in the figure is simply a feature unique to this  
 565 storm. While the exact time development of the storm is not captured well, the general  
 566 scales of GICs are matched well, as is the differentiation between quiet and active times.

567 In summary, prediction of geoelectric field magnitudes can be achieved with rea-  
 568 sonable accuracy (POD of at least 35% even at the highest event threshold), but the pre-  
 569 diction of elevated levels of GICs proves difficult with any approach used. The LSTMs  
 570 usually outperform the persistence models, except in the bias, where the persistence model  
 571 has the benefit of being statistically equivalent to the data it is being compared to. The  
 572 persistence model also generally has a lower POFD and higher HSS value at low thresh-  
 573 olds (e.g. TH=30 V/km for LSTM-E) because quiet periods tend to persist over time.  
 574 The LSTMs, however, outperform persistence at the higher thresholds, which are more  
 575 important for forecasting purposes.

## 576 5 Discussion

577 We have attempted to forecast GICs from solar wind data using LSTMs with two  
 578 different approaches. We now look at some of the reasons behind the particular difficulty  
 579 in forecasting GICs.

580 Some of the low skill seen when comparing predictions to GIC measurements is down  
 581 to four reasons, mostly related to our GIC data: firstly, there is noise in the GIC obser-  
 582 vations, particularly at SS1, which has a consistent level of 1 A noise during the day -  
 583 this is not predicted by the model. Secondly, GIC observations until 2021 had a max-  
 584 imum cutoff point of 3.4 A in the positive direction, removing some peaks from our event  
 585 list, and these have not been accounted for. Thirdly, the model struggles to predict the  
 586 direction of the geoelectric field values, which are likely driven by smaller-scale ionospheric  
 587 currents (Dimmock et al., 2020). Fourthly, as noted in Sec. 2.3, the peaks of observed  
 588 GICs are often underestimated by geophysical modelling, meaning peaks in the GIC mea-  
 589 surements after the cut-off level was removed were often much larger than modelled. This  
 590 is a problem related to the geoelectric field modelling that may affect the LSTM’s abil-  
 591 ity to learn the problem due to insufficient accuracy in the field modelling. While minute  
 592 cadence data does capture most of the variability in the GICs, the lack of higher frequency  
 593 content appears to be the primary cause of underestimated peaks, a problem discussed be-  
 594 fore in Grawe et al. (2018) and recently for the specific problem of GIC estimates in Beggan  
 595 et al. (2021). As such, it is not surprising that the LSTMs tend to underestimate the ac-  
 596 tual GICs, and a correction would have to be applied to the target data to account for  
 597 this.

598 Outside of the data-specific problems, there are also some timing errors, meaning  
 599 some peaks arrived slightly later or earlier than they were observed, and as such are not  
 600 logged as correct predictions even though an event threshold was crossed.

601 In an application of the model in operations, one caveat is that the maximum pos-  
 602 sible forecast is 200 mV/km due to a self-imposed limit to improve the model’s ability  
 603 to learn. We assume that in practise, this would be negligible because all values above  
 604 a certain level (e.g. 100 mV/km) would be of interest, regardless of how large they be-  
 605 come. As also discussed in Wintoft et al. (2016), the scale of geomagnetic variations dur-  
 606 ing extreme events can theoretically become so large that it is effectively unbounded for  
 607 the purpose of this discussion. In the future, this 200 mV/km limit could be improved  
 608 on by training a model specifically for large value forecasting, which can be switched to  
 609 if the original model forecasts  $E > 150$  mV/km.

610 In an ideal case, a forecasting model would be developed while taking a cost-loss  
 611 analysis (Murphy, 1977) such as that used in a space weather context in Owens et al.  
 612 (2014) into consideration. In the case of network protection, this is a very complex sce-  
 613 nario due to the varying impacts and costs associated with transformer damage or power

614 grid outage, many of which are currently nearly impossible to estimate. This is some-  
 615 thing that can hopefully be developed further as studies into GIC risk progress (Eastwood  
 616 et al., 2018).

617 Another, more general problem in forecasting any measure of ground geomagnetic  
 618 activity from solar wind measurements without further input from magnetospheric mod-  
 619 elling is that not all geomagnetic variations are driven by the solar wind directly (see e.g.  
 620 Kamide et al., 1998; Eastwood et al., 2015). Many variations will result from reconec-  
 621 tion in the magnetotail and chaotic processes and would not be relatable through our  
 622 model, which is essentially a coupling function from the solar wind at the bow shock to  
 623 the geoelectric field in Austria. Although the machine learning approach described here  
 624 works at a basic level and could be more promising than forecasts of  $dB/dt$  alone, it would  
 625 need to be coupled with either data from space-borne monitors observing the Earth's  
 626 magnetosphere, more complex physical models of magnetospheric behaviour, or both to  
 627 escape this limitation.

628 The calculations and measurements of the GICs shown in this study are for a spe-  
 629 cific grid configuration, even though the power grid is continually being upgraded and  
 630 changed. These changes can have large effects on individual GIC scales over long time  
 631 ranges. The results shown in Table 1 extend far into the past, for which we do not have  
 632 a detailed history of grid changes, so the values listed could have been much smaller or  
 633 much larger depending on how the grid was set up. For the LSTM predictions, we have  
 634 conducted our analysis with the comparison to measurements over a considerably shorter  
 635 time range of a few years, where the grid has not changed to any great degree, but the  
 636 predictions may not be valid in the future for a different grid configuration. In this case,  
 637 a new fit would need to be found for Eq. 1, and either the LSTM-GIC model would need  
 638 to be retrained on the updated GIC data, or the GIC values could be calculated anew  
 639 from the otherwise unchanged LSTM-E output.

640 Our aim was to develop a model that can provide useful forecasts for power grid  
 641 operators by providing estimates of the scales of GICs. The difference between this and  
 642 former studies such as Lotz et al. (2017) and Honkonen et al. (2018), who also predicted  
 643 ground geoelectric fields from solar wind data, is that we have approached the problem  
 644 with a new tool (a recurrent neural network) and have been able to forecast GICs di-  
 645 rectly along with the geoelectric field, with the results compared to measured GICs. We  
 646 have had some success, particularly with forecasting the geoelectric field, and have tried  
 647 forecasting substation-specific GICs for the first time, but there are still many problems  
 648 to be addressed to turn this method into a useful forecast.

## 649 6 Summary

650 We have developed a machine learning approach to forecast GICs in Austria. Us-  
 651 ing data from the past 26 years and the 2003 Halloween storm as a case study, we ar-  
 652 gued that forecasts of  $dB/dt$  alone, which have been the focus of most past studies, are  
 653 not sufficient to make actionable GIC forecasts.

654 From this initial analysis, we set out to forecast maximum expected GICs (over a  
 655 forty minute window) either directly for specific substations in the power grid or more  
 656 generally from forecasts of the regional geoelectric field components. From a small set  
 657 of initial machine learning approaches, an LSTM (recurrent neural network) with an At-  
 658 tention mechanism showed the most promise in forecasting skill and this was developed  
 659 into a more complex approach.

660 A selection of models were trained on 21 years of geoelectric field values modelled  
 661 from geomagnetic variations at the geomagnetic observatory in Fürstenfeldbruck close  
 662 to Austria. In the first method, two recurrent neural networks or LSTMs were trained  
 663 to predict the northward and eastward modelled geoelectric field components and com-

664 pute the specific substation GICs using a linear equation. In the second method, an LSTM  
 665 was trained to predict modelled GICs at two substations, which we know correlate very  
 666 well with the measurements. Five years of data were reserved for testing and evaluat-  
 667 ing the model. The results were compared to DC measurements at two substations in  
 668 the Austrian power grid.

669 The LSTM model worked with reasonable success when predicting the geoelectric  
 670 field modelled from geomagnetic variations, although translating this success into good  
 671 GIC forecasts proved difficult. It was possible, however, to outperform a model that sim-  
 672 ply takes the last observed GICs to forecast future values.

673 We conclude that forecasting the GICs observed in the power grid from solar wind  
 674 data measured at L1 is a difficult task, even when the forecasting model does a reason-  
 675 able job of forecasting the geoelectric field components or modelled GIC. There are many  
 676 ways to improve the modelling in the future, including using higher-resolution magnetic  
 677 field measurements (or applying a correction to the modelled geoelectric field before train-  
 678 ing) to more accurately estimate the peak geoelectric field and GIC values, and by in-  
 679 cluding information on the development of the magnetosphere during storm times.

680 Although this study has looked specifically at a mid-latitude region, where geomag-  
 681 netic variations and GICs are not as large as those seen in higher latitude regions such  
 682 as Scandinavia, we have been able to compare model output directly to measurements  
 683 and expect that the conclusions drawn will also be valid for other regions with GICs at  
 684 different scales.

685 A lower-resolution version of the LSTM-E model will be coupled with the PRED-  
 686 STORM solar wind forecast (Bailey et al., 2020), which provides forecasts of the ambi-  
 687 ent solar wind a few days in advance, based on either a recurrence model or data from  
 688 a spacecraft east of the Sun-Earth line such as STEREO or a future mission to the La-  
 689 grange 5 point. We also plan in the future to integrate methods on solar wind  $B_z$  fore-  
 690 casting (Reiss et al., 2021) or CME flux rope modelling (Weiss et al., 2021) to advance  
 691 our capabilities in GIC forecasting for any type of solar wind structures.

## 692 7 Data Availability

- 693 • INTERMAGNET data for FUR and WIC:  
 694 <https://intermagnet.org/data-donnee/download-eng.php>
- 695 • OMNI data: [https://spdf.gsfc.nasa.gov/pub/data/omni/high\\_res\\_omni/](https://spdf.gsfc.nasa.gov/pub/data/omni/high_res_omni/)
- 696 • Open source code for this work (in Python 3 and Jupyter Notebook form):  
 697 <https://github.com/bairaelyn/SOLARWIND2GIC> (Note: Zenodo DOI will fol-  
 698 low for final version.)
- 699 • Exact details on the LSTM structure and hyperparameters used for training can  
 700 be found in the supporting information for this study.

## 701 Acknowledgments

702 The results presented in this paper rely on the data collected at the Conrad Observa-  
 703 tory (ZAMG) in Austria and at Fürstfeldbruck (LMU), Germany. We thank the Ludwig-  
 704 Maximilians-Universität München for supporting its operation and INTERMAGNET  
 705 for promoting high standards of magnetic observatory practice ([www.intermagnet.org](http://www.intermagnet.org)).  
 706 The data used in this study is publicly available (with the exception of the measurements  
 707 of GICs in Austria), and details on where to find the data can be found in Section 7. We  
 708 thank Ilja Honkonen for providing the results from his 2018 study for comparison. R.L.B.,  
 709 C.M., M.A.R., and A.J.W. thank the Austrian Science Fund (FWF) for research fund-  
 710 ing from projects P31659-N27 and P31521-N27. C.D.B. was funded under UK Natural  
 711 Environment Research Council Grant NE/P017231/1 “Space Weather Impact on Ground-

712 based Systems (SWIGS)”. We thank the two anonymous reviewers for their careful read-  
 713 ings of this manuscript and helpful suggestions.

## 714 References

- 715 Ádám, A., Prácser, E., & Wesztergom, V. (2012). Estimation of the electric resist-  
 716 tivity distribution (EURHOM) in the European lithosphere in the frame of the  
 717 EURISGIC WP2 project. *Acta Geodaetica et Geophysica Hungarica*, *47*(4),  
 718 377-387.
- 719 Bahdanau, D., Cho, K., & Bengio, Y. (2015). Neural machine translation by jointly  
 720 learning to align and translate. In *3rd international conference on learning rep-  
 721 resentations*.
- 722 Bailey, R. L., Halbedl, T. S., Schattauer, I., Achleitner, G., & Leonhardt, R. (2018).  
 723 Validating GIC models with measurements in Austria: evaluation of accuracy  
 724 and sensitivity to input parameters. *Space Weather*.
- 725 Bailey, R. L., Halbedl, T. S., Schattauer, I., Römer, A., Achleitner, G., Beggan,  
 726 C. D., ... Leonhardt, R. (2017). Modelling geomagnetically induced cur-  
 727 rents in midlatitude Central Europe using a thin-sheet approach. *Annales  
 728 Geophysicae*, *35*(3), 751.
- 729 Bailey, R. L., Möstl, C., Reiss, M. A., Weiss, A. J., Amerstorfer, U. V., Amerstorfer,  
 730 T., ... Leonhardt, R. (2020). Prediction of Dst during solar minimum using in  
 731 situ measurements at I5. *Space Weather*, *18*(5), e2019SW002424.
- 732 Baker, D. N., Li, X., Pulkkinen, A., Ngwira, C. M., Mays, M. L., Galvin, A. B., &  
 733 Simunac, K. D. C. (2013, October). A major solar eruptive event in July 2012:  
 734 Defining extreme space weather scenarios. *Space Weather*, *11*(10), 585-591.  
 735 doi: 10.1002/swe.20097
- 736 Barbosa, C., Alves, L., Caraballo, R., Hartmann, G. A., Papa, A. R., & Pirjola,  
 737 R. J. (2015). Analysis of geomagnetically induced currents at a low-latitude  
 738 region over the solar cycles 23 and 24: comparison between measurements and  
 739 calculations. *Journal of Space Weather and Space Climate*, *5*, A35.
- 740 Beggan, C. D., Richardson, G. S., Baillie, O., Hübert, J., & Thomson, A. W. (2021).  
 741 Geoelectric field measurement, modelling and validation during geomagnetic  
 742 storms in the uk. *Journal of Space Weather and Space Climate*, *11*, 37.
- 743 Bhaskar, A., & Vichare, G. (2019). Forecasting of SYMH and ASYH indices for  
 744 geomagnetic storms of solar cycle 24 including St. Patrick’s day, 2015 storm  
 745 using NARX neural network. *J. Space Weather Space Clim.*, *9*, A12.
- 746 Bloomfield, D. S., Higgins, P. A., McAteer, R. T. J., & Gallagher, P. T. (2012,  
 747 Mar). Toward Reliable Benchmarking of Solar Flare Forecasting Methods. *The  
 748 Astrophysical Journal Letters*, *747*(2), L41.
- 749 Bolduc, L. (2002). GIC observations and studies in the Hydro-Québec power system.  
 750 *Journal of Atmospheric and Solar-Terrestrial Physics*, *64*(16), 1793–1802.
- 751 Boteler, D. H., & Pirjola, R. J. (2017). Modeling geomagnetically induced currents.  
 752 *Space Weather*, *15*(1), 258-276.
- 753 Boteler, D. H., Pirjola, R. J., & Nevanlinna, H. (1998). The effects of geomagnetic  
 754 disturbances on electrical systems at the Earth’s surface. *Advances in Space  
 755 Research*, *22*, 17-27.
- 756 Butala, M. D., Kazerooni, M., Makela, J. J., Kamalabadi, F., Gannon, J. L., Zhu,  
 757 H., & Overbye, T. J. (2017). Modeling geomagnetically induced currents from  
 758 magnetometer measurements: Spatial scale assessed with reference measure-  
 759 ments. *Space Weather*, *15*(10), 1357-1372.
- 760 Caraballo, R., González-Esparza, J. A., Sergeeva, M., & Pacheco, C. R. (2020).  
 761 First GIC estimates for the Mexican power grid. *Space Weather*, *18*(2),  
 762 e2019SW002260.
- 763 Chave, A. D., & Jones, A. G. (2012). *The magnetotelluric method: Theory and prac-  
 764 tice*. Cambridge University Press.

- 765 Dimmock, A. P., Rosenqvist, L., Welling, D. T., Viljanen, A., Honkonen, I., Boynton,  
766 R. J., & Yordanova, E. (2020). On the regional variability of db/dt and  
767 its significance to gic. *Space Weather*, *18*(8), e2020SW002497.
- 768 Eastwood, J., Hapgood, M., Biffis, E., Benedetti, D., Bisi, M., Green, L., ... Bur-  
769 nett, C. (2018). Quantifying the economic value of space weather forecasting  
770 for power grids: An exploratory study. *Space Weather*, *16*(12), 2052-2067.
- 771 Eastwood, J., Hietala, H., Toth, G., Phan, T., & Fujimoto, M. (2015). What con-  
772 trols the structure and dynamics of Earth's magnetosphere? *Space Science Re-*  
773 *views*, *188*(1), 251-286.
- 774 Galassi, A., Lippi, M., & Torroni, P. (2020). Attention in natural language process-  
775 ing. *IEEE Transactions on Neural Networks and Learning Systems*.
- 776 Gaunt, C. T., & Coetzee, G. (2007). Transformer failures in regions incorrectly con-  
777 sidered to have low GIC-risk. In *Power tech, 2007 IEEE Lausanne* (p. 807-812).  
778 IEEE.
- 779 Gil, A., Modzelewska, R., Moskwa, S., Siluszyk, A., Siluszyk, M., Wawrzynczak,  
780 A., & Zakrzewska, S. (2019). Does time series analysis confirms the relation-  
781 ship between space weather effects and the failures of electrical grids in south  
782 poland? *Journal of Mathematics in Industry*, *9*(1), 1-16.
- 783 Gopalswamy, N., Yashiro, S., Liu, Y., Michalek, G., Vourlidas, A., Kaiser, M. L.,  
784 & Howard, R. A. (2005, September). Coronal mass ejections and other  
785 extreme characteristics of the 2003 October-November solar eruptions.  
786 *Journal of Geophysical Research (Space Physics)*, *110*(A9), A09S15. doi:  
787 10.1029/2004JA010958
- 788 Grawe, M. A., Makela, J. J., Butala, M. D., & Kamalabadi, F. (2018). The impact  
789 of magnetic field temporal sampling on modeled surface electric fields. *Space*  
790 *Weather*, *16*(11), 1721-1739.
- 791 Heidke, P. (1926). Berechnung des erfolges und der güte der windstärkevorhersagen  
792 im sturmwarnungsdienst. *Geografiska Annaler*, *8*(4), 301-349.
- 793 Honkonen, I., Kuvshinov, A., Rastätter, L., & Pulkkinen, A. (2018). Predicting  
794 global ground geoelectric field with coupled geospace and three-dimensional  
795 geomagnetic induction models. *Space Weather*, *16*(8), 1028-1041.
- 796 Juusola, L., Viljanen, A., van de Kamp, M., Tanskanen, E. I., Vanhamäki, H., Par-  
797 tamies, N., & Kauristie, K. (2015). High-latitude ionospheric equivalent  
798 currents during strong space storms: Regional perspective. *Space Weather*,  
799 *13*(1), 49-60.
- 800 Kamide, Y., Baumjohann, W., Daglis, I. A., Gonzalez, W. D., Grande, M., Jose-  
801 lyn, J. A., ... Vasyliunas, V. M. (1998). Current understanding of magnetic  
802 storms: Storm-substorm relationships. *Journal of Geophysical Research: Space*  
803 *Physics*, *103*(A8), 17705-17728.
- 804 Keesee, A. M., Pinto, V., Coughlan, M., Lennox, C., Mahmud, M. S., & Connor,  
805 H. K. (2020). Comparison of deep learning techniques to model connections  
806 between solar wind and ground magnetic perturbations. *Frontiers in Astron-*  
807 *omy and Space Sciences*, *7*, 72.
- 808 Kelbert, A. (2020). The role of global/regional earth conductivity models in natural  
809 geomagnetic hazard mitigation. *Surv Geophys*, *41*, 115-166.
- 810 Liu, Y. D., Luhmann, J. G., Kajdič, P., Kilpua, E. K. J., Lugaz, N., Nitta, N. V., ...  
811 Galvin, A. B. (2014, March). Observations of an extreme storm in interplan-  
812 etary space caused by successive coronal mass ejections. *Nature Communica-*  
813 *tions*, *5*, 3481. doi: 10.1038/ncomms4481
- 814 Lotz, S., & Cilliers, P. (2015). A solar wind-based model of geomagnetic field fluc-  
815 tuations at a mid-latitude station. *Advances in Space Research*, *55*(1), 220 -  
816 230.
- 817 Lotz, S., & Danskin, D. W. (2017). Extreme value analysis of induced geoelectric  
818 field in South Africa. *Space Weather*, *15*(10), 1347-1356.
- 819 Lotz, S., Heyns, M., & Cilliers, P. J. (2017). Regression-based forecast model of in-

- duced geoelectric field. *Space Weather*, 15(1), 180-191.
- Lu, J., Peng, Y., Wang, M., Gu, S., & Zhao, M. (2016). Support Vector Machine combined with distance correlation learning for Dst forecasting during intense geomagnetic storms. *Planetary and Space Science*, 120, 48 - 55.
- Molinski, T. S. (2002). Why utilities respect geomagnetically induced currents. *Journal of atmospheric and solar-terrestrial physics*, 64(16), 1765-1778.
- Murphy, A. H. (1977). The value of climatological, categorical and probabilistic forecasts in the cost-loss ratio situation. *Monthly Weather Review*, 105(7), 803-816.
- Ngwira, C. M., Pulkkinen, A., Leila Mays, M., Kuznetsova, M. M., Galvin, A., Simunac, K., ... Glocer, A. (2013). Simulation of the 23 July 2012 extreme space weather event: What if this extremely rare CME was Earth directed? *Space Weather*, 11(12), 671-679.
- Ngwira, C. M., Pulkkinen, A. A., Bernabeu, E., Eichner, J., Viljanen, A., & Crowley, G. (2015). Characteristics of extreme geoelectric fields and their possible causes: Localized peak enhancements. *Geophysical Research Letters*, 42(17), 6916-6921.
- Owens, M. J., Horbury, T. S., Wicks, R. T., McGregor, S. L., Savani, N. P., & Xiong, M. (2014). Ensemble downscaling in coupled solar wind-magnetosphere modeling for space weather forecasting. *Space Weather*, 12(6), 395-405.
- Owens, M. J., Lockwood, M., Barnard, L. A., Scott, C. J., Haines, C., & Macneil, A. (2021, May). Extreme Space-Weather Events and the Solar Cycle. *Solar Physics*, 296(5), 82. doi: 10.1007/s11207-021-01831-3
- Price, P. R. (2002). Geomagnetically induced current effects on transformers. *IEEE Transactions on Power Delivery*, 17(4), 1002-1008.
- Pulkkinen, A., Bernabeu, E., Thomson, A., Viljanen, A., Pirjola, R., Boteler, D., ... MacAlester, M. (2017). Geomagnetically induced currents: Science, engineering, and applications readiness. *Space Weather*, 15(7), 828-856.
- Pulkkinen, A., Hesse, M., Habib, S., Van der Zel, L., Damsky, B., Policelli, F., ... Creamer, E. (2010). Solar shield: forecasting and mitigating space weather effects on high-voltage power transmission systems. *Natural hazards*, 53(2), 333-345.
- Pulkkinen, A., Hesse, M., Kuznetsova, M., & Rastätter, L. (2007). First-principles modeling of geomagnetically induced electromagnetic fields and currents from upstream solar wind to the surface of the Earth. *Annales Geophysicae*, 25(4), 881-893.
- Pulkkinen, A., Pirjola, R., & Viljanen, A. (2007). Determination of ground conductivity and system parameters for optimal modeling of geomagnetically induced current flow in technological systems. *Earth, planets and space*, 59(9), 999-1006.
- Pulkkinen, A., Rastatter, L., Kuznetsova, M., Singer, H., Balch, C., Weimer, D., ... Weigel, R. (2013, June). Community-wide validation of geospace model ground magnetic field perturbation predictions to support model transition to operations. *Space Weather*, 11(6), 369-385.
- Pulkkinen, A., Taktakishvili, A., Odstreil, D., & Jacobs, W. (2009). Novel approach to geomagnetically induced current forecasts based on remote solar observations. *Space Weather*, 7(8).
- Pulkkinen, A., Viljanen, A., & Pirjola, R. (2006). Estimation of geomagnetically induced current levels from different input data. *Space Weather*, 4(8).
- Reiss, M. A., Möstl, C., Bailey, R. L., Rüdissler, H. T., Amerstorfer, U. V., Amerstorfer, T., ... Windisch, A. (2021, August). Machine learning for predicting the Bz magnetic field component from upstream in situ observations of solar coronal mass ejections. *arXiv e-prints*, arXiv:2108.04067.
- Shepherd, S. G. (2014). Altitude-adjusted corrected geomagnetic coordinates: Definition and functional approximations. *Journal of Geophysical Research: Space*

- 875 *Physics*, 119(9), 7501-7521.
- 876 Sun, R., & Balch, C. (2019). Comparison between 1-D and 3-D geoelectric field  
877 methods to calculate geomagnetically induced currents: A case study. *IEEE*  
878 *Transactions on Power Delivery*, 34(6), 2163-2172.
- 879 Svanda, Michal, Mourenas, Didier, Zertová, Karla, & Výbost'oková, Tatiana. (2020).  
880 Immediate and delayed responses of power lines and transformers in the Czech  
881 electric power grid to geomagnetic storms. *J. Space Weather Space Clim.*, 10,  
882 26.
- 883 Tasistro-Hart, A., Grayver, A., & Kuvshinov, A. (2021). Probabilistic geomagnetic  
884 storm forecasting via deep learning. *Journal of Geophysical Research: Space*  
885 *Physics*, 126(1), e2020JA028228.
- 886 Torta, J. M., Serrano, L., Regué, J. R., Sánchez, A. M., & Roldán, E. (2012). Ge-  
887 omagnetically induced currents in a power grid of northeastern Spain. *Space*  
888 *Weather*, 10(6).
- 889 Viljanen, A., Pirjola, R., Prácsér, E., Katkalov, J., & Wik, M. (2014). Geomagnet-  
890 ically induced currents in Europe - modelled occurrence in a continent-wide  
891 power grid. *J. Space Weather Space Clim.*, 4, A09.
- 892 Weigel, R. S. (2017). A comparison of methods for estimating the geoelectric field.  
893 *Space Weather*, 15(2), 430-440.
- 894 Weiss, A. J., Möstl, C., Amerstorfer, T., Bailey, R. L., Reiss, M. A., Hinterreiter, J.,  
895 ... Bauer, M. (2021). Analysis of coronal mass ejection flux rope signatures  
896 using 3DCORE and approximate Bayesian Computation. *The Astrophysical*  
897 *Journal Supplement Series*, 252(1), 9.
- 898 Welling, D. T., Ngwira, C. M., Opgenoorth, H., Haiducek, J. D., Savani, N. P., Mor-  
899 ley, S. K., ... Liemohn, M. (2018). Recommendations for next-generation  
900 ground magnetic perturbation validation. *Space Weather*, 16(12), 1912-1920.
- 901 Wilks, D. S. (2011). *Statistical methods in the atmospheric sciences*. Amsterdam;  
902 Boston: Elsevier Academic Press.
- 903 Wintoft, P. (2005, July). Study of the solar wind coupling to the time difference hor-  
904 izontal geomagnetic field. *Annales Geophysicae*, 23(5), 1949-1957.
- 905 Wintoft, P., Viljanen, A., & Wik, M. (2016). Extreme value analysis of the time  
906 derivative of the horizontal magnetic field and computed electric field. *Annales*  
907 *Geophysicae*, 34(4), 485-491.
- 908 Wintoft, P., & Wik, M. (2021). Exploring three recurrent neural network architec-  
909 tures for geomagnetic predictions. *Frontiers in Astronomy and Space Sciences*,  
910 8, 72.
- 911 Wintoft, P., Wik, M., & Viljanen, A. (2015). Solar wind driven empirical forecast  
912 models of the time derivative of the ground magnetic field. *Journal of Space*  
913 *Weather and Space Climate*, 5, A7.
- 914 Zhang, J. J., Wang, C., Sun, T. R., Liu, C. M., & Wang, K. R. (2015). GIC due  
915 to storm sudden commencement in low-latitude high-voltage power network in  
916 China: Observation and simulation. *Space Weather*, 13(10), 643-655.